PHYSICAL REVIEW B **102**, 064506 (2020)

Magnetic switching in Weyl semimetal-superconductor heterostructures

Narayan Mohanta,[1,*] A. Taraphder,[2] Elbio Dagotto,[1,3] and Satoshi Okamoto[1]
[1]*Material Science and Technology Division, Oak Ridge National Laboratory, Oak Ridge, Tennessee 37831, USA*
[2]*Department of Physics and Center for Theoretical Studies, Indian Institute of Technology Kharagpur, W.B. 721302, India*
[3]*Department of Physics and Astronomy, The University of Tennessee, Knoxville, Tennessee 37996, USA*

(Received 19 November 2019; revised 17 May 2020; accepted 30 July 2020; published 17 August 2020)

We present a switching mechanism that utilizes the proximity coupling between the surface spin texture of a Weyl semimetal and a superconductor in a Weyl semimetal-superconductor Weyl semimetal trilayer heterostructure. We show that the superconductivity in the middle layer can be fully suppressed by the surface spin texture of the Weyl semimetals in the presence of an external magnetic field, but it can be recovered again by only changing the field direction. The restoration of the middle-layer superconductivity indicates a sharp transition to a low-resistance state. This sharp switching effect, realizable using a Weyl semimetal because of its strong spin-momentum locking and surface spin polarization, is a promising avenue for novel superconducting spin-valve applications.

DOI: 10.1103/PhysRevB.102.064506

I. INTRODUCTION

A three-dimensional Weyl semimetal (WSM) is strikingly different from other classes of materials with nontrivial band topology because of the presence of surface Fermi arcs [1,2], which prompted the observation of a plethora of intriguing properties, such as quantum oscillations in magnetoresistance [3–5] and chiral magnetic effect [6–18]. The Fermi arcs exhibit a spin texture with a strong spin-momentum locking which leads to a spin polarization (up to 80% for TaAs) on the surface of the WSMs [19–21]. By introducing a superconducting gap in the WSM, the superconductor (SC) inherits the nontrivial topology of the electronic structure of the WSM, giving rise to unconventional properties such as finite-momentum pairing and Majorana zero modes [22–34]. At a WSM/SC interface, superconductivity is proposed to be induced by the proximity effect inside the WSM near the interface [35]. Despite a few studies on the proximity effect of the superconductivity inside the WSM in a WSM/SC interface, the *inverse* proximity effect of the WSM surface magnetization on the superconductivity remains unexplored.

In this paper, we demonstrate a switching effect induced by the interplay between superconductivity and magnetization at a WSM/SC interface, in the presence of an external magnetic field. We consider a trilayer heterostructure, with an *s*-wave SC sandwiched between two WSM slabs in such a way that the top and bottom WSMs have opposite alignments of the Fermi arcs. In this geometry, the WSM surfaces, on both sides of the SC, have a net spin polarization *in the same direction*. The superconductivity in the middle SC layer is suppressed completely by the joint pair-breaking effect of the WSM surface magnetization and the magnetic field. However, by rotating the field, the net magnetization of the WSM surfaces drops to a smaller value and the fully suppressed superconductivity restores again, indicating a sharp transition to the zero-resistance state in the middle SC layer. Such a magnetic switching has the potential to advance the spin-valve applications that at present employ trilayer heterostructures of ferromagnets (FMs) and SCs [36–52].

In the state-of-the-art spin-valve switching devices, involving a FM(hard)/SC/FM(soft) trilayer, as shown in Fig. 1(a), the resistance R_p, in the parallel polarization of the top and bottom FMs near the superconducting transition temperature T_c, is larger than the resistance R_{ap} in the antiparallel case. The magnetic field flips the polarization in the soft FM and produces a transition to a low-resistance state. In our proposed WSM-based geometry, shown in Figs. 1(b) and 1(c), the net magnetization of the WSM surfaces on both sides of the SC drops to a smaller value when the magnetic field is applied opposite to the spin polarization direction. The field rotation drives the middle SC to the zero-resistance state, implying a low resistance in the WSM/SC/WSM trilayer.

II. MODEL AND METHOD

We consider a type-I WSM with broken time-reversal symmetry and two Weyl points, described by the following Hamiltonian [53]:

$$\mathcal{H}_w = \sum_{\mathbf{k}} -[\{m(2-\cos k_y-\cos k_z)+2t_x(\cos k_x-\cos k_0)\}\sigma_x - (2t\sin k_y)\sigma_y-(2t\sin k_z)\sigma_z-\mu_w\mathcal{I}], \quad (1)$$

written in the basis $(c_{\mathbf{k},\uparrow}, c_{\mathbf{k},\downarrow})^T$, m, t_x, and t describe the bulk band dispersion, μ_w is the chemical potential, $\boldsymbol{\sigma} \equiv (\sigma_x, \sigma_y, \sigma_z)$ are the Pauli matrices acting on the pseudospins, $\mathcal{I}$ is the 2×2 identity matrix, and $\mathbf{k} \equiv (k_x, k_y, k_z)$ denotes the momentum inside the WSM. The Weyl nodes are located at $(\pm k_0, 0, 0)$ as depicted in Fig. 1(d). In Figs. 1(e) and 1(f), we show the Fermi

---

[*] mohantan@ornl.gov

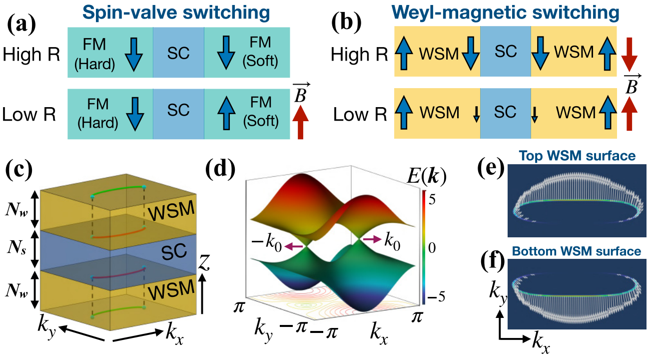

FIG. 1. (a) Standard spin-valve switching mechanism involving a FM/SC/FM trilayer. The blue arrows denote the magnetization in the FMs. (b) Proposed switching mechanism using a WSM/SC/WSM trilayer. The blue arrows denote the net surface magnetization. (c) Schematic of the considered trilayer heterostructure. The red and green lines at the surfaces of the WSMs denote the conjugate Fermi arcs. (d) Bulk bands of a WSM with broken time-reversal symmetry, showing the pair of the Weyl nodes at $(\pm k_0,0,0)$. $E(\mathbf{k})$ are the eigenvalues of Hamiltonian Eq. (1) at $k_z=0$ (in units of t, a parameter mentioned in the text). (e), (f) The computed Fermi arcs [the momentum-resolved density of states at energy $E(\mathbf{k}) = -0.3t$] and spin textures (white arrows) on the opposite surfaces of an isolated WSM slab of thickness $N_w = 15$.

arcs and the spin texture on the opposite surfaces of an isolated WSM slab [54]. The parameters $t=1$, $m=2t$, $k_0=\pi/2$, $t_x=t$, used in Ref. [53], are kept fixed, with no qualitative change in our conclusions for other choices.

We consider BCS-type electron pairing in the middle SC slab, expressed by the following Hamiltonian [54]:

$$\mathcal{H}_s = -\sum_{\mathbf{k},\sigma}[2t_s(\cos k_x+\cos k_y+\cos k_z)+\mu_s]d^\dagger_{\mathbf{k},\sigma}d_{\mathbf{k},\sigma} + \sum_{\mathbf{k}}(U_0\Delta_s d^\dagger_{\mathbf{k},\uparrow}d^\dagger_{-\mathbf{k},\downarrow} + \text{H.c.}) + NU_0\Delta_s^2, \qquad (2)$$

where t_s is the hopping amplitude, μ_s the chemical potential, $\Delta_s=\langle d_{\mathbf{k},\uparrow}d_{-\mathbf{k},\downarrow}\rangle$ the s-wave pairing amplitude in the SC, U_0 the pairwise attractive interaction strength, and N is the total number of momenta in the Brillouin zone. We set $t_s=1.5t$ and $U_0=-t_s$ everywhere, without losing generality.

The Hamiltonian for the heterostructure is constructed by transforming the Hamiltonians $\mathcal{H}_w$ and $\mathcal{H}_s$ into the slab geometry [54,55], with N_s layers in the SC slab and N_w layers in both (top and bottom) WSM slabs. Open boundary conditions are imposed only along the stacking direction (the z axis), so k_x and k_y are good quantum numbers for the description in each layer.

The coupling between the WSM and the SC slabs at the WSM/SC interfaces is described by the following tunneling Hamiltonian:

$$\mathcal{H}_{\text{tun}} = -\sum_{\mathbf{k}^{\parallel},l_z,\sigma}(t_{\text{tun}}c^\dagger_{\mathbf{k}^{\parallel},\sigma,l_z}d_{\mathbf{k}^{\parallel},\sigma,l_z+1} + \text{H.c.}), \qquad (3)$$

where l_z is the vertical layer index at the interface, t_{tun} is the tunneling amplitude between the WSMs and the SC and $\mathbf{k}^{\parallel} \equiv (k_x,k_y)$ is the momentum in the k_x-k_y plane.

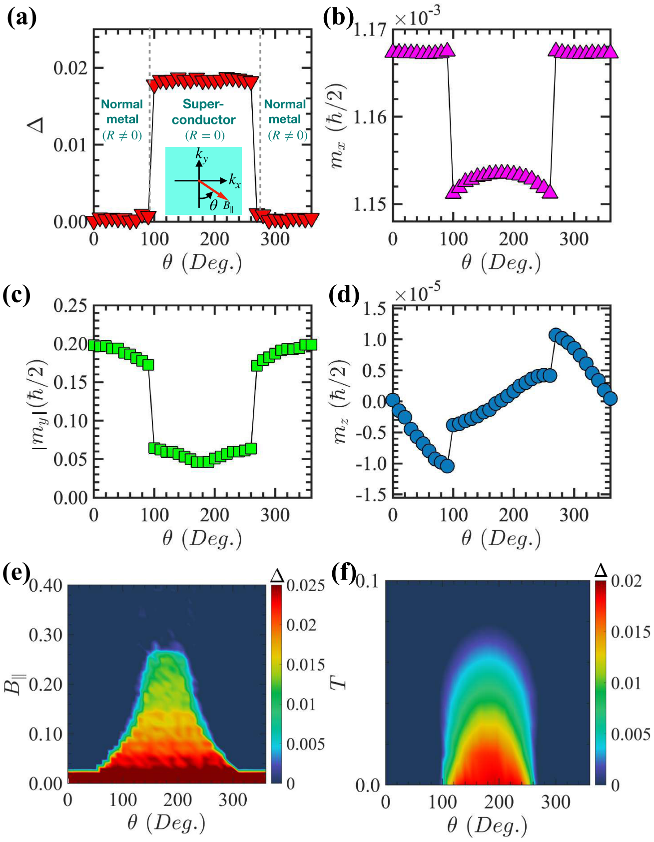

FIG. 2. (a) Superconducting pairing amplitude Δ, averaged over all layers of the WSM/SC/WSM heterostructure, plotted as a function of the magnetic-field angle θ which is measured with respect to the $-k_y$ direction, as shown in the inset. (b)–(d) θ variation of the magnetization components m_x, m_y, m_z at the bottom surface of the top WSM slab. The magnetic field and the temperature in plots (a)–(d) are $B_\parallel=0.1t$ and $T=0$, respectively. (e), (f) Variation of Δ (number in the color bar) with the angle θ and the magnetic-field amplitude $B_\parallel$ (at $T=0$) in (e), and temperature T (at $B_\parallel=0.1t$) in (f). Parameters used are $N_w=15$, $N_s=15$, $t_{tun}=t$, $\mu_w=-0.3t$, and $\mu_s=0.1t$.

The external magnetic field, applied uniformly in all the layers of the heterostructure, is included as a Zeeman exchange coupling to the pseudospins,

$$\mathcal{H}_z = \sum_{\mathbf{k}^{\parallel},l_z,\sigma,\sigma'}(\mathbf{B}\cdot\boldsymbol{\sigma}_{\sigma\sigma'})c^\dagger_{\mathbf{k}^{\parallel},\sigma,l_z}c_{\mathbf{k}^{\parallel},\sigma',l_z}, \qquad (4)$$

where $\mathbf{B}=(B_\parallel\cos\theta', B_\parallel\sin\theta', 0)$, $B_\parallel$ is the strength of the magnetic field, $\theta'=3\pi/2+\theta$, and θ is the field angle as shown in Fig. 2(a). Henceforth, all energies are expressed in units of the parameter t defined in Eq. (1).

The pairing amplitude in each layer l_z inside the SC slab is obtained self-consistently using $\Delta_{s,l_z}=\langle d_{\mathbf{k}^{\parallel},l_z,\uparrow}d_{-\mathbf{k}^{\parallel},l_z,\downarrow}\rangle$ [54]. The proximity-induced s-wave pairing amplitude inside the WSM slab is calculated via $\Delta_{w,l_z}=\langle c_{\mathbf{k}^{\parallel},l_z,\uparrow}c_{-\mathbf{k}^{\parallel},l_z,\downarrow}\rangle$. Although a small finite-momentum pairing and a triplet pairing could also be induced in the WSM, we focus only on singlet pairing at zero center-of-mass momentum which is the dominant pairing channel and relevant to the present paper. The average pairing amplitude for the heterostructure is then obtained via $\Delta=[1/(N_s+2N_w)]\sum_{l_z}(\Delta_{s,l_z}+\Delta_{w,l_z})$. The spin texture at a layer l_z ($m_{\mathbf{k}^\parallel,x}$, $m_{\mathbf{k}^\parallel,y}$, $m_{\mathbf{k}^\parallel,z}$) is obtained by computing the spin-expectation values at each momentum $\mathbf{k}^\parallel$ and the average magnetization components (m_x, m_y, m_z) are obtained by taking the average in the two-dimensional Brillouin zone [54].

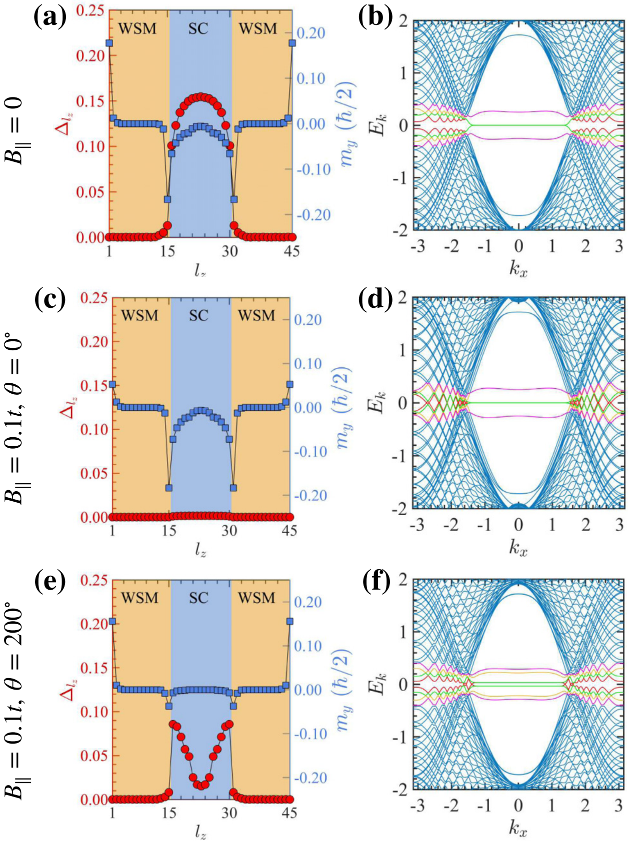

FIG. 3. (a), (c), (e) Variation of the superconducting pairing amplitude Δ_{l_z} (left vertical axis) and y component of magnetization m_y (right vertical axis) with the layer index l_z at (a) magnetic field $B_\parallel = 0$, (c) $B_\parallel = 0.1t$, $\theta = 0°$, and (e) $B_\parallel = 0.1t$, $\theta = 200°$. (b), (d), and (f) show the corresponding energy spectrum of the WSM/SC/WSM heterostructure at $k_y = 0$. The energy levels in red, green, yellow, and magenta originate primarily from the surfaces of the WSMs. Parameters are the same as in Fig. 2.

III. ORIGIN OF THE MAGNETIC SWITCHING

The main concept introduced here, the magnetic switching at the WSM/SC interfaces, involves the strong interplay between superconductivity and the WSM surface magnetization; the latter competes against the electron pairing near the interfaces. The magnetic field $B_\parallel$=0.1t ($< B_\parallel^c \approx 0.3t$, the critical field for the SC), applied along θ=0°, cooperates with the WSM surface magnetization to *completely* suppress superconductivity. Remarkably, by changing the field direction, the average pairing amplitude Δ re-emerges and jumps from nearly zero to a finite value at $\theta \approx 100°$. The order parameter Δ remains almost constant within a range $100° \lesssim \theta \lesssim 260°$, as shown in Fig. 2(a). This sudden restoration of the superconductivity, only by changing the field angle, implies a switching from a finite-resistance to a low-resistance state. *This magnetic field-driven "switching" is the main finding of this paper.*

To understand the origin of this switching effect, we explore the θ dependence of the magnetization components. Interestingly, we find similar discontinuous jumps in the magnetization components at the WSM terminating layers, adjacent to the SC slab, as shown in Figs. 2(b)–2(d). The in-plane magnetization components m_x and m_y drop to relatively smaller values within the same range $100° \lesssim \theta \lesssim 260°$. The out-of-plane component m_z also undergoes sharp transitions at the critical field angles $\theta_{c1} \approx 100°$ and $\theta_{c2} \approx 260°$, as shown in Fig. 2(d). This finding underlines the strong interplay between the magnetism in the WSM surface and the superconductivity near the WSM/SC interfaces. The θ variation of Δ with the field amplitude $B_\parallel$, in Fig. 2(e), suggests that there is a lower and upper critical field and the switching occurs in between. The lower critical field is the required field to fully suppress the superconductivity at certain ranges of θ values, while the upper critical field is the largest field above which the reappearance of superconductivity is unanticipated. Temperature variation of Δ, in Fig. 2(f), suggests that the switching effect appears predominantly at low temperatures, below the superconducting T_c of the middle SC.

To explore the interplay between the WSM surface magnetization and the superconductivity, we plot the layer-resolved pairing amplitude Δ_{l_z}(=Δ_{s,l_z} or Δ_{w,l_z}), and the dominant magnetization component m_y, in Figs. 3(a), 3(c) and 3(e), at different field scenarios and the corresponding spectrum in Figs. 3(b), 3(d) and 3(f). At $B_\parallel$=0, a small pairing amplitude is induced inside the WSMs, by proximity effect, but this induced superconductivity is limited to the near vicinity of the interfaces [35]. Conversely, the pairing amplitude inside the SC is also suppressed near the interfaces since the WSM surface magnetism penetrates inside the SC and affects the superconductivity. At a finite magnetic field $B_\parallel$=0.1t, applied along θ=0°, the superconductivity is completely suppressed, as shown in Fig. 3(c), by the combined pair-breaking effect of the magnetic field and the WSM surface magnetization. However, when the field is applied along θ=200°, i.e., opposite to the WSM surface magnetization, the net magnetization of the WSM surface drops drastically, which enables the reappearance of the superconductivity inside the SC, as depicted in Fig. 3(e). Similar reappearance of the superconductivity takes place within the angle range $100° \lesssim \theta \lesssim 260°$. The profile of Δ_{l_z} remains nearly unchanged within this range of θ [54]. The sharp transitions, at the critical angles, is possible in a WSM because of its strong spin-momentum locking which makes the spin texture of the Fermi arcs quite robust against the external magnetic field, applied at an angle outside this angle range. Within this range, the magnetic field overcomes the spin-momentum locking and significantly reduces the in-plane magnetization components [54].

The energy spectrum of the heterostructure at $B_\parallel$=0, in Fig. 3(b), shows that two pairs of energy levels (green and red) exhibit flat zero-energy states within the Fermi-arc region ($|k_x| \lesssim k_0$) while two other pairs (magenta and yellow) are gapped out at finite energies. These low-energy bands originate from the hybridization between the surface states in

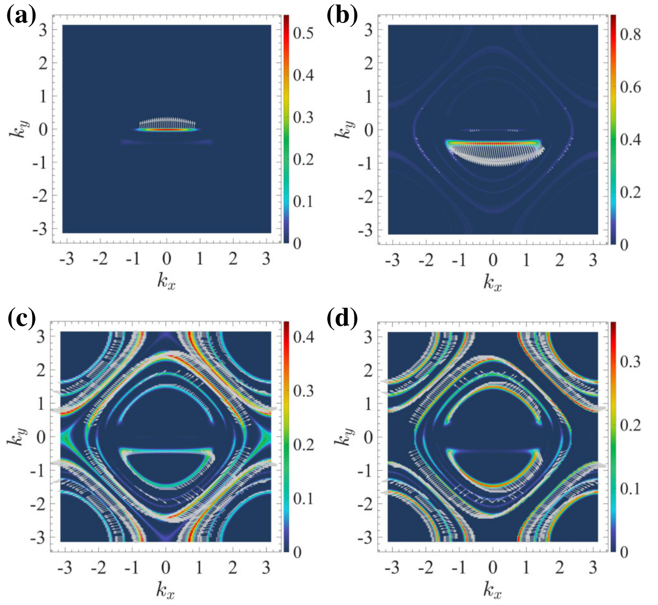

FIG. 4. Momentum-resolved density of states $A(\mathbf{k}^{\parallel},E)$ (color bar) and spin texture (arrows show the in-plane spin-expectation values $m_{\mathbf{k}^{\parallel},x}$ and $m_{\mathbf{k}^{\parallel},y}$) at energy $E=-0.3t$ at zero magnetic field and different layers of the WSM/SC/WSM heterostructure. (a) $l_z=1$ (top layer of the top WSM), (b) $l_z=15$ (bottom layer of the top WSM), (c) $l_z=16$ (top layer of the SC), (d) $l_z=18$ (inside the SC but close to the top WSM/SC interface). Parameters are the same as in Fig. 2.

the WSMs and the SC slabs. The spectrum changes when a magnetic field $B_{\parallel}=0.1t$ is applied along $\theta=0^{\circ}$, as shown in Fig. 3(d). Particularly, outside the flat-band region ($|k_x|>k_0$), the red and the green bands do not have an energy gap at $\theta=0^{\circ}$ [Fig. 3(d)] and a finite energy gap at $\theta=200^{\circ}$ [Fig. 3(f)]. These two angles belong to the two different states viz. the suppressed and recovered superconducting states, shown before in Fig. 2(a). Evidently, the electronic spectra also reveals a signature of these different states.

To gain insight on the critical field angles θ_{c1} and θ_{c2}, we calculated the spin texture and the momentum-resolved density of states $A(\mathbf{k}^{\parallel},E)=\sum_{\sigma,\lambda}|c_{\mathbf{k}^{\parallel},\sigma,l_z}|^2\delta(E\text{-}E_{\mathbf{k}^{\parallel}\lambda})+|c^{\dagger}_{-\mathbf{k}^{\parallel},\sigma,l_z}|^2\delta(E+E_{-\mathbf{k}^{\parallel}\lambda})$ at different layers of the heterostructure ($c_{\mathbf{k}^{\parallel},\sigma,l_z}$ is replaced by $d_{\mathbf{k}^{\parallel},\sigma,l_z}$ for the SC layers). In Fig. 4, we show the spin texture at four different layers at $B_{\parallel}=0$. The top surface of the top WSM ($l_z=1$) reveals a Fermi arc and spin texture [Fig. 4(a)] at energy $E=-0.3t(=\mu_w)$, similar to the case of an isolated WSM slab, shown earlier in Fig. 1(e). On the other hand, Fig. 4(d), shows the constant-energy contours and spin texture at a SC layer ($l_z=18$), slightly below the top WSM/SC interface, at energy $E=-0.3t$ ($<\mu_s$) showing the electronlike and holelike contours. Notably, two electronlike contours around $\mathbf{k}^{\parallel}=\mathbf{0}$ are disconnected along the $k_y=0$ direction, influenced by the Fermi arc in the neighboring WSM layer ($l_z=15$). The proximity effect of the Fermi arc is prominent at the top SC layer ($l_z=16$) [in Fig. 4(c)] which also develops a Fermi arc in the central disjoint electronlike contour with its spin texture originating from the adjacent WSM surface [in Fig. 4(b)]. The spin texture at the top WSM/SC interface (both $l_z=15$ and $l_z=16$) results in a net spin polarization, as shown in Figs. 4(b) and 4(c). This spin polarization suppresses the superconductivity near the WSM/SC interfaces and drives the switching transitions.

IV. DISCUSSION

Here, we discuss briefly the robustness of the proposed switching effect against different parameter choices in our model, the most relevant one being the hopping energy t_{tun} between the WSM and the SC. The results presented until now were obtained with $t_{\text{tun}}=t$ at SC-layer thickness $N_s=15$. In Fig. 5, we show the layer-resolved pairing amplitude Δ_{l_z} at different values of t_{tun} and N_s. Each plot shows the variation in Δ_{l_z} with the magnetic field angle θ and the layer index l_z. These results support the main finding, i.e., there are two distinct ranges of θ viz. the suppressed (off) and the enhanced (on) superconducting states. The profile of Δ_{l_z} remains nearly unchanged within the angle range $100^{\circ}\leqslant\theta\leqslant 260^{\circ}$ (at $N_s=15$ and $t_{\text{tun}}=t$). Though there is a profile of the superconducting gap inside the SC slab, the entire SC slab is superconducting, implying a zero-resistance state inside it. The switching effect is, therefore, achievable at different t_{tun}, the smallest being $t_{\text{tun}}=0.5t$ at which the switching in the superconducting state appears when N_s is equal to or below $N_s=9$. We further assert that the switching effect at even smaller t_{tun} than $t_{\text{tun}}=0.5t$ can be achieved by concomitantly reducing the SC slab thickness N_s because t_{tun} relates with the length scale of the proximity effect.

The coexistence of the spin polarization and the superconductivity is observed at metallic point contacts in TaAs [34]. Our analysis on the lattice matching at different WSM/SC interfaces and experimental findings of a strong interface coupling suggest that the switching effect can be tested at Nb/TaP, Nb/NbP, In/NbP, and In/TaP interfaces [33,54,56]. The strength of the external magnetic field is smaller than the critical field of the SC (≈ 0.4 T for Nb [57]). The switching effect can be further tuned by the chemical potential in the SC slab [54].

The potential advantages of the proposed WSM-based switching mechanism over the existing mechanisms are the following. In the existing FM-based switching devices, the presence of Néel domains leads to the coexistence of both standard ($R_p>R_{ap}$) and inverse ($R_p<R_{ap}$) switching effects [47]. In the proposed WSM-based switching mechanism, the unanticipated coexistence of the standard and the inverse switching effects is not possible because the spin textures on the Fermi arcs, which are fixed in a given WSM, are robust due to strong spin-momentum locking and, therefore, they are expected to be free from any domain structure. Also, the strong spin-momentum locking and the weak Coulomb interaction in WSMs such as TaAs or NbAs ensure a sharp switching, free from the Coulomb-drag or magneto-Coulomb effect that causes trouble in existing FM-based devices [58–60].

To conclude, we predicted a magnetic-switching mechanism in WSM/SC/WSM heterostructures, which employs the strong spin-momentum locking and the surface spin polarization of the WSMs. We showed that a sharp switching

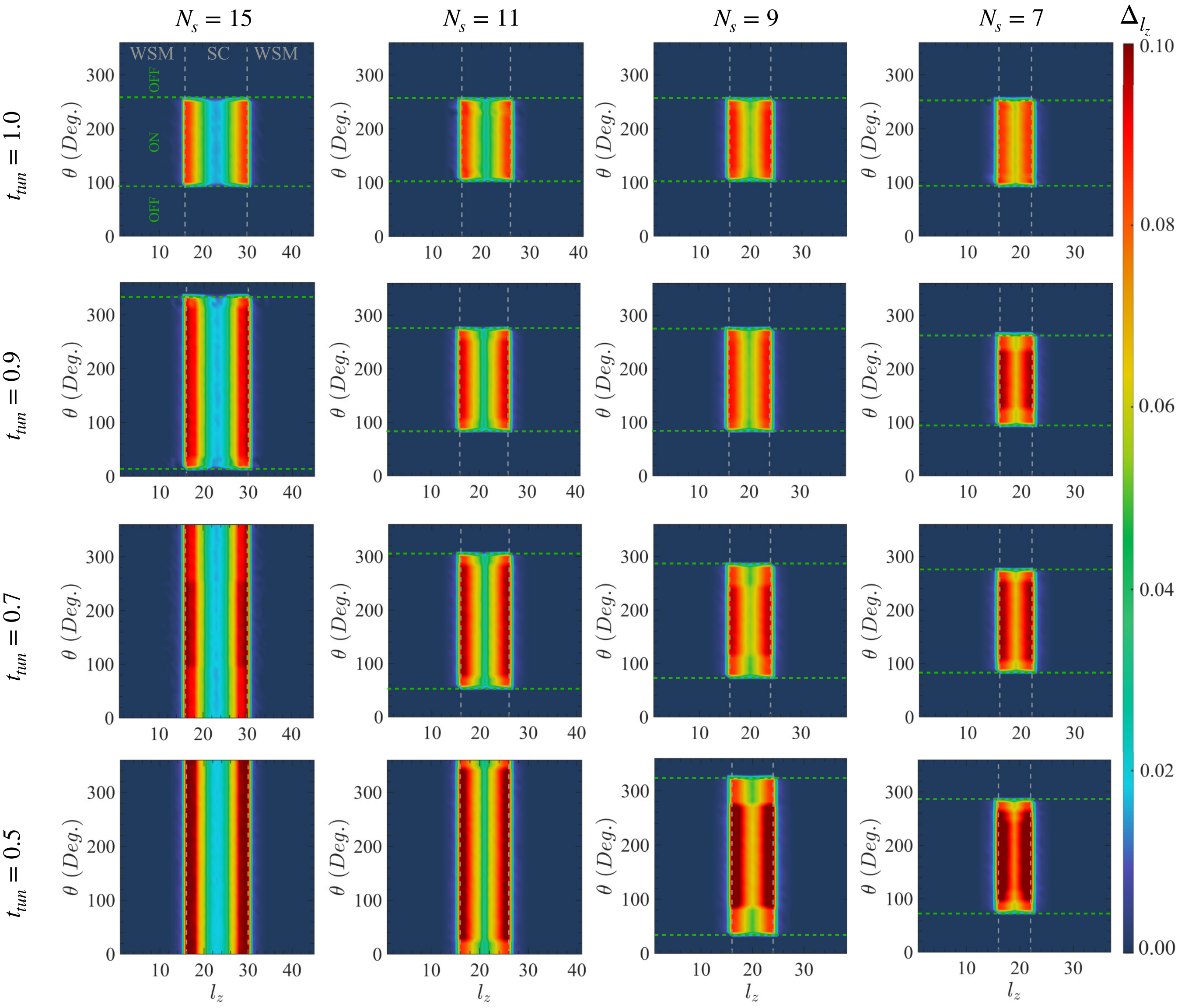

FIG. 5. Profiles of the layer-resolved pairing amplitude Δ_{l_z} (in the l_z-θ plane) at different hopping energies t_{tun} and the SC layer thicknesses N_s. The applied magnetic field is $B = 0.1t$ and other parameters are the same as in Fig. 2. The on (off) region in the top-left panel shows the magnetic-field angle range within which the middle SC region is superconducting (nonsuperconducting), implying a low-resistance state in the trilayer heterostructure.

phenomenon arises due to the interplay between the WSM surface magnetization, superconductivity, and the external magnetic field. The switching effect is testable using a WSM with either broken time-reversal symmetry or broken both inversion and time-reversal symmetries and has the potential for novel spin-valve applications.

ACKNOWLEDGMENTS

N.M. acknowledges discussions with A. Matos-Abiague. This work was supported by the U.S. Department of Energy (DOE), Office of Science, Basic Energy Sciences (BES), Materials Sciences and Engineering Division.

[1] B. Q. Lv, S. Muff, T. Qian, Z. D. Song, S. M. Nie, N. Xu, P. Richard, C. E. Matt, N. C. Plumb, L. X. Zhao, G. F. Chen, Z. Fang, X. Dai, J. H. Dil, J. Mesot, M. Shi, H. M. Weng, and H. Ding, Observation of Fermi-Arc Spin Texture in TaAs, Phys. Rev. Lett. **115**, 217601 (2015).

[2] Y. Sun, S.-C. Wu, and B. Yan, Topological surface states and Fermi arcs of the noncentrosymmetric Weyl semimetals TaAs, TaP, NbAs, and NbP, Phys. Rev. B **92**, 115428 (2015).

[3] A. C. Potter, I. Kimchi, and A. Vishwanath, Quantum oscillations from surface Fermi arcs in Weyl and Dirac semimetals, Nat. Commun. **5**, 5161 (2014).

[4] P. J. W. Moll, N. L. Nair, T. Helm, A. C. Potter, I. Kimchi, A. Vishwanath, and J. G. Analytis, Transport evidence for

Fermi-arc-mediated chirality transfer in the Dirac semimetal $Cd_3 As_2$, Nature **535**, 266 (2016).

[5] P. J. W. Moll, A. C. Potter, N. L. Nair, B. J. Ramshaw, K. A. Modic, S. Riggs, B. Zeng, N. J. Ghimire, E. D. Bauer, R. Kealhofer, F. Ronning, and J. G. Analytis, Magnetic torque anomaly in the quantum limit of Weyl semimetals, Nat. Commun. **7**, 12492 (2016).

[6] H. B. Nielsen and M. Ninomiya, The Adler-Bell-Jackiw anomaly and Weyl fermions in a crystal, Phys. Lett. B **130**, 389 (1983).

[7] D. T. Son and B. Z. Spivak, Chiral anomaly and classical negative magnetoresistance of Weyl metals, Phys. Rev. B **88**, 104412 (2013).

[8] H.-J. Kim, K.-S. Kim, J.-F. Wang, M. Sasaki, N. Satoh, A. Ohnishi, M. Kitaura, M. Yang, and L. Li, Dirac Versus Weyl Fermions in Topological Insulators: Adler-Bell-Jackiw Anomaly in Transport Phenomena, Phys. Rev. Lett. **111**, 246603 (2013).

[9] A. A. Burkov, Chiral Anomaly and Diffusive Magnetotransport in Weyl Metals, Phys. Rev. Lett. **113**, 247203 (2014).

[10] C.-Z. Li, L.-X. Wang, H. Liu, J. Wang, Z.-M. Liao, and D.-P. Yu, Giant negative magnetoresistance induced by the chiral anomaly in individual $Cd_3 As_2$ nanowires, Nat. Commun. **6**, 10137 (2015).

[11] X. Huang, L. Zhao, Y. Long, P. Wang, D. Chen, Z. Yang, H. Liang, M. Xue, H. Weng, Z. Fang, X. Dai, and G. Chen, Observation of the Chiral-Anomaly-Induced Negative Magnetoresistance in 3D Weyl Semimetal TaAs, Phys. Rev. X **5**, 031023 (2015).

[12] Q. Li, D. E. Kharzeev, C. Zhang, Y. Huang, I. Pletikosic, A. V. Fedorov, R. D. Zhong, J. A. Schneeloch, G. D. Gu, and T. Valla, Chiral magnetic effect in $ZrTe_5$, Nat. Phys. **12**, 550 (2016).

[13] Y. Li, L. Li, J. Wang, T. Wang, X. Xu, C. Xi, C. Cao, and J. Dai, Resistivity plateau and negative magnetoresistance in the topological semimetal $TaSb_2$, Phys. Rev. B **94**, 121115 (2016).

[14] Z. Wang, Y. Zheng, Z. Shen, Y. Lu, H. Fang, F. Sheng, Y. Zhou, X. Yang, Y. Li, C. Feng, and Z.-A. Xu, Helicity-protected ultrahigh mobility Weyl fermions in NbP, Phys. Rev. B **93**, 121112 (2016).

[15] J. Klotz, S.-C. Wu, C. Shekhar, Y. Sun, M. Schmidt, M. Nicklas, M. Baenitz, M. Uhlarz, J. Wosnitza, C. Felser, and B. Yan, Quantum oscillations and the Fermi surface topology of the Weyl semimetal NbP, Phys. Rev. B **93**, 121105 (2016).

[16] P. Baireuther, J. A. Hutasoit, J. Tworzydło, and C. W. J. Beenakker, Scattering theory of the chiral magnetic effect in a Weyl semimetal: Interplay of bulk Weyl cones and surface Fermi arcs, New J. Phys. **18**, 045009 (2016).

[17] K. Taguchi, T. Imaeda, M. Sato, and Y. Tanaka, Photovoltaic chiral magnetic effect in Weyl semimetals, Phys. Rev. B **93**, 201202 (2016).

[18] Y.-T. Lin, L.-J. Zhai, and C.-Y. Mou, Scaling of the chiral magnetic effect in quantum diffusive Weyl semimetals, Phys. Rev. B **97**, 245121 (2018).

[19] P. Li, W. Wu, Y. Wen, C. Zhang, J. Zhang, S. Zhang, Z. Yu, S. A. Yang, A. Manchon, and X.-x. Zhang, Spin-momentum locking and spin-orbit torques in magnetic nano-heterojunctions composed of Weyl semimetal WTe_2, Nat. Commun. **9**, 3990 (2018).

[20] S.-Y. Xu, I. Belopolski, D. S. Sanchez, M. Neupane, G. Chang, K. Yaji, Z. Yuan, C. Zhang, K. Kuroda, G. Bian, C. Guo, H. Lu, T.-R. Chang, N. Alidoust, H. Zheng, C.-C. Lee, S.-M. Huang, C.-H. Hsu, H.-T. Jeng, A. Bansil, T. Neupert, F. Komori, T. Kondo, S. Shin, H. Lin, S. Jia, and M. Z. Hasan, Spin Polarization and Texture of the Fermi Arcs in the Weyl Fermion Semimetal TaAs, Phys. Rev. Lett. **116**, 096801 (2016).

[21] B. Feng, Y.-H. Chan, Y. Feng, R.-Y. Liu, M.-Y. Chou, K. Kuroda, K. Yaji, A. Harasawa, P. Moras, A. Barinov, W. Malaeb, C. Bareille, T. Kondo, S. Shin, F. Komori, T.-C. Chiang, Y. Shi, and I. Matsuda, Spin texture in type-II Weyl semimetal WTe_2, Phys. Rev. B **94**, 195134 (2016).

[22] G. Y. Cho, J. H. Bardarson, Y.-M. Lu, and J. E. Moore, Superconductivity of doped Weyl semimetals: Finite-momentum pairing and electronic analog of the ^{3}He-A phase, Phys. Rev. B **86**, 214514 (2012).

[23] G. Bednik, A. A. Zyuzin, and A. A. Burkov, Superconductivity in Weyl metals, Phys. Rev. B **92**, 035153 (2015).

[24] P. Hosur, X. Dai, Z. Fang, and X.-L. Qi, Time-reversal-invariant topological superconductivity in doped Weyl semimetals, Phys. Rev. B **90**, 045130 (2014).

[25] T. Meng and L. Balents, Weyl superconductors, Phys. Rev. B **86**, 054504 (2012).

[26] A. Chen and M. Franz, Superconducting proximity effect and Majorana flat bands at the surface of a Weyl semimetal, Phys. Rev. B **93**, 201105 (2016).

[27] P. Baireuther, J. Tworzydło, M. Breitkreiz, İ. Adagideli, and C. W. J. Beenakker, Weyl-Majorana solenoid, New J. Phys. **19**, 025006 (2017).

[28] Y. Qi, P. G. Naumov, M. N. Ali, C. R. Rajamathi, W. Schnelle, O. Barkalov, M. Hanfland, S.-C. Wu, C. Shekhar, Y. Sun, V. Süß, M. Schmidt, U. Schwarz, E. Pippel, P. Werner, R. Hillebrand, T. Förster, E. Kampert, S. Parkin, R. J. Cava, C. Felser, B. Yan, and S. A. Medvedev, Superconductivity in Weyl semimetal candidate $MoTe_2$, Nat. Commun. **7**, 11038 (2016).

[29] P. Lu, J.-S. Kim, J. Yang, H. Gao, J. Wu, D. Shao, B. Li, D. Zhou, J. Sun, D. Akinwande, D. Xing, and J.-F. Lin, Origin of superconductivity in the Weyl semimetal WTe_2 under pressure, Phys. Rev. B **94**, 224512 (2016).

[30] F. C. Chen, X. Luo, R. C. Xiao, W. J. Lu, B. Zhang, H. X. Yang, J. Q. Li, Q. L. Pei, D. F. Shao, R. R. Zhang, L. S. Ling, C. Y. Xi, W. H. Song, and Y. P. Sun, Superconductivity enhancement in the S-doped Weyl semimetal candidate $MoTe_2$, Appl. Phys. Lett. **108**, 162601 (2016).

[31] H. Wang, H. Wang, Y. Chen, J. Luo, Z. Yuan, J. Liu, Y. Wang, S. Jia, X.-J. Liu, J. Wei, and J. Wang, Discovery of tip induced unconventional superconductivity on Weyl semimetal, Sci. Bull. **62**, 425 (2017).

[32] Z. Guguchia, F. von Rohr, Z. Shermadini, A. T. Lee, S. Banerjee, A. R. Wieteska, C. A. Marianetti, B. A. Frandsen, H. Luetkens, Z. Gong, S. C. Cheung, C. Baines, A. Shengelaya, G. Taniashvili, A. N. Pasupathy, E. Morenzoni, S. J. L. Billinge, A. Amato, R. J. Cava, R. Khasanov, and Y. J. Uemura, Signatures of the topological s+- superconducting order parameter in the type-II Weyl semimetal Td-$MoTe_2$, Nat. Commun. **8**, 1082 (2017).

[33] M. D. Bachmann, N. Nair, F. Flicker, R. Ilan, T. Meng, N. J. Ghimire, E. D. Bauer, F. Ronning, J. G. Analytis, and P. J. W. Moll, Inducing superconductivity in Weyl semimetal microstructures by selective ion sputtering, Sci. Adv. **3**, e1602983 (2017).

[34] L. Aggarwal, S. Gayen, S. Das, R. Kumar, V. Süß, C. Felser, C. Shekhar, and G. Sheet, Mesoscopic superconductivity and high

spin polarization coexisting at metallic point contacts on Weyl semimetal TaAs, Nat. Commun. **8**, 13974 (2017).

[35] U. Khanna, A. Kundu, S. Pradhan, and S. Rao, Proximity-induced superconductivity in Weyl semimetals, Phys. Rev. B **90**, 195430 (2014).

[36] V. S. Speriosu, J. P. Nozieres, B. A. Gurney, B. Dieny, T. C. Huang, and H. Lefakis, Role of interfacial mixing in giant magnetoresistance, Phys. Rev. B **47**, 11579 (1993).

[37] J. S. Moodera, J. Nowak, and R. J. M. van de Veerdonk, Interface Magnetism and Spin Wave Scattering in Ferromagnet-Insulator-Ferromagnet Tunnel Junctions, Phys. Rev. Lett. **80**, 2941 (1998).

[38] A. I. Buzdin, A. V. Vedyayev, and N. V. Ryzhanova, Spin-orientation-dependent superconductivity in F/S/F structures, Europhys. Lett. **48**, 686 (1999).

[39] L. R. Tagirov, Low-Field Superconducting Spin Switch Based on a Superconductor Ferromagnet Multilayer, Phys. Rev. Lett. **83**, 2058 (1999).

[40] S. Takahashi, H. Imamura, and S. Maekawa, Spin Imbalance and Magnetoresistance in Ferromagnet/Superconductor/Ferromagnet Double Tunnel Junctions, Phys. Rev. Lett. **82**, 3911 (1999).

[41] I. Baladié, A. Buzdin, N. Ryzhanova, and A. Vedyayev, Interplay of superconductivity and magnetism in superconductor/ferromagnet structures, Phys. Rev. B **63**, 054518 (2001).

[42] J. Y. Gu, C.-Y. You, J. S. Jiang, J. Pearson, Ya. B. Bazaliy, and S. D. Bader, Magnetization-Orientation Dependence of the Superconducting Transition Temperature in the Ferromagnet-Superconductor-Ferromagnet System: CuNi/Nb/CuNi, Phys. Rev. Lett. **89**, 267001 (2002).

[43] A. Potenza and C. H. Marrows, Superconductor-ferromagnet CuNi/Nb/CuNi trilayers as superconducting spin-valve core structures, Phys. Rev. B **71**, 180503 (2005).

[44] V. Peña, Z. Sefrioui, D. Arias, C. Leon, J. Santamaria, J. L. Martinez, S. G. E. te Velthuis, and A. Hoffmann, Giant Magnetoresistance in Ferromagnet/Superconductor Superlattices, Phys. Rev. Lett. **94**, 057002 (2005).

[45] A. Yu. Rusanov, S. Habraken, and J. Aarts, Inverse spin switch effects in ferromagnet-superconductor-ferromagnet trilayers with strong ferromagnets, Phys. Rev. B **73**, 060505 (2006).

[46] I. K. Yanson, Yu. G. Naidyuk, V. V. Fisun, A. Konovalenko, O. P. Balkashin, L. Yu. Triputen, and V. Korenivski, Surface spin-valve effect, Nano Lett. **7**, 927 (2007).

[47] J. Zhu, X. Cheng, C. Boone, and I. N. Krivorotov, Origin of the Inverse Spin Switch Effect in Superconducting Spin Valves, Phys. Rev. Lett. **103**, 027004 (2009).

[48] J. Salafranca and S. Okamoto, Unconventional Proximity Effect and Inverse Spin-Switch Behavior in a Model Manganite-Cuprate-Manganite Trilayer System, Phys. Rev. Lett. **105**, 256804 (2010).

[49] G. De Simoni, E. Strambini, J. S. Moodera, F. S. Bergeret, and F. Giazotto, Toward the absolute spin-valve effect in superconducting tunnel junctions, Nano Lett. **18**, 6369 (2018).

[50] K. Halterman, O. T. Valls, and M. Alidoust, Spin-Controlled Superconductivity and Tunable Triplet Correlations in Graphene Nanostructures, Phys. Rev. Lett. **111**, 046602 (2013).

[51] L. Majidi and R. Asgari, Valley- and spin-switch effects in molybdenum disulfide superconducting spin valve, Phys. Rev. B **90**, 165440 (2014).

[52] M. Alidoust and K. Halterman, Half-metallic superconducting triplet spin multivalves, Phys. Rev. B **97**, 064517 (2018).

[53] T. M. McCormick, I. Kimchi, and N. Trivedi, Minimal models for topological Weyl semimetals, Phys. Rev. B **95**, 075133 (2017).

[54] See Supplemental Material at http://link.aps.org/supplemental/10.1103/PhysRevB.102.064506 for more information.

[55] N. Mohanta, A. P. Kampf, and T. Kopp, Emergent momentum-space skyrmion texture on the surface of topological insulators, Sci. Rep. **7**, 45664 (2017).

[56] G. Grabecki, A. Dąbrowski, P. Iwanowski, A. Hruban, B. J. Kowalski, N. Olszowska, J. Kołodziej, M. Chojnacki, K. Dybko, A. Łusakowski, T. Wojtowicz, T. Wojciechowski, R. Jakieła, and A. Wiśniewski, Conductance spectra of (Nb, Pb, In)/NbP superconductor/Weyl semimetal junctions, Phys. Rev. B **101**, 085113 (2020).

[57] W. H. Butler, Upper Critical Field of Nb: Calculated Temperature Dependence and Anisotropy, Phys. Rev. Lett. **44**, 1516 (1980).

[58] G. Vignale, Observing the spin coulomb drag in spin-valve devices, Phys. Rev. B **71**, 125103 (2005).

[59] S. J. van der Molen, N. Tombros, and B. J. van Wees, Magneto-Coulomb effect in spin-valve devices, Phys. Rev. B **73**, 220406 (2006).

[60] D. D. Hiep, M. Tanaka, and P. N. Hai, Inverse spin-valve effect in nanoscale si-based spin-valve devices, J. Appl. Phys. **122**, 223904 (2017).